

A *CHANDRA* AND *HST* VIEW OF *WISE*-SELECTED AGN CANDIDATES IN DWARF GALAXIES

LILIKOI J. LATIMER

eXtreme Gravity Institute, Department of Physics, Montana State University, Bozeman, MT 59717, USA

AMY E. REINES

eXtreme Gravity Institute, Department of Physics, Montana State University, Bozeman, MT 59717, USA

KEVIN N. HAINLINE

Steward Observatory, University of Arizona, 933 North Cherry Avenue, Tucson, AZ 85721, USA

JENNY E. GREENE

Department Astrophysical Sciences, Princeton University, Princeton, NJ 08544, USA

DANIEL STERN

Jet Propulsion Laboratory, California Institute of Technology, 4800 Oak Grove Drive, Mail Stop 169-221, Pasadena, CA 91109, USA

Draft version June 25, 2022

ABSTRACT

Reliably identifying active galactic nuclei (AGNs) in dwarf galaxies is key to understanding black hole demographics at low masses and constraining models for black hole seed formation. Here we present *Chandra X-ray Observatory* observations of eleven dwarf galaxies that were chosen as AGN candidates using *Wide-field Infrared Survey Explorer* (*WISE*) mid-infrared (mid-IR) color-color selection. *Hubble Space Telescope* images are also presented for ten of the galaxies. Based on Sloan Digital Sky Survey spectroscopy, six galaxies in our sample have optical evidence for hosting AGNs and five are classified as star-forming. We detect X-ray point sources with luminosities above that expected from X-ray binaries in the nuclei of five of the six galaxies with optical evidence of AGNs. However, the X-ray emission from these AGNs is generally much lower than expected based on AGN scaling relations with infrared and optical tracers. We do not find compelling evidence for AGNs in the five optically-selected star-forming galaxies despite having red mid-IR colors. Only two are detected in X-rays and their properties are consistent with stellar-mass X-ray binaries. Based on this multiwavelength study, we conclude that two-color mid-IR AGN diagnostics at the resolution of *WISE* cannot be used to reliably select AGNs in optically-star-forming dwarf galaxies. Future observations in the infrared with the *James Webb Space Telescope* offer a promising path forward.

Keywords: galaxies: active — galaxies: dwarf — galaxies: nuclei — X-rays: galaxies

1. INTRODUCTION

The vast majority of massive galaxies play host to supermassive black holes (BHs) at their cores. However, we do not know how these monster BHs came to be. Ideally, we would directly observe galaxies in the early Universe and the “seed” BHs they harbor, but these BHs currently remain out of observational reach. They are simply too distant and faint to detect with existing facilities (e.g., Volonteri & Reines 2016; Vito et al. 2018). Instead, we turn to nearby dwarf galaxies. These galaxies are relatively low mass ($M_{\star} \lesssim 10^{9.5} M_{\odot}$) and may host BHs of similar mass to those in early-universe galaxies (for reviews, see Reines & Comastri 2016; Mezcua 2017; Greene et al. 2020). We can use the occupation fraction of massive BHs in these proxy galaxies as well as scaling relations at low mass to help distinguish between different theories concerning the formation of seed BHs such as remnants from Pop III stars, stellar mergers in compact star clusters, or direct collapse of protogalactic

gas (Volonteri 2010; van Wassenhove et al. 2010; Greene 2012; Ricarte & Natarajan 2018).

There is now growing evidence for the existence of BHs in dwarf galaxies, with detailed studies of single galaxies to large-scale surveys (e.g. Reines et al. 2011, 2013, 2014, 2020; Baldassare et al. 2015, 2016, 2017; Baldassare et al. 2018; Baldassare et al. 2020; Mezcua et al. 2018, 2019; Mezcua & Sánchez 2020; Schramm et al. 2013; Moran et al. 2014; Lemons et al. 2015; Hainline et al. 2016; Pardo et al. 2016; Dickey et al. 2019; Nguyen et al. 2019; Latimer et al. 2019; Schutte et al. 2019; Birchall et al. 2020; Lupi et al. 2020). Multiple studies have tried to make progress identifying massive BHs in the mid-infrared (mid-IR) using data from the *Wide-field Infrared Survey Explorer* (*WISE*) (Wright et al. 2010) by extrapolating active galactic nuclei (AGN) diagnostics (e.g. Jarrett et al. 2011; Stern et al. 2012) to low-mass galaxies (Satyapal et al. 2014; Sartori et al. 2015; Marleau et al. 2017). These studies find that the IR-selected AGN fraction seems to increase at low galaxy masses, a puzzling conclusion that contradicts studies at other wavelengths. Motivated by these results, as well as earlier work (e.g.,

with *WISE*) that revealed extreme star-forming dwarf galaxies could produce very red mid-IR colors (Hirashita & Hunt 2004; Reines et al. 2008; Griffith et al. 2011; Izotov et al. 2011, 2014; Rémy-Ruyer et al. 2015; O’Connor et al. 2016), Hainline et al. (2016) revisited mid-IR AGN selection techniques applied to dwarf galaxies.

Hainline et al. (2016) find that dwarf galaxies with the reddest mid-IR colors have the youngest stellar populations and highest star formation rates, demonstrating that dwarf galaxies can heat dust in a way that can mimic luminous AGNs. In particular, they show that using a single $W1 - W2$ color cut to select candidate AGNs leads to severe contamination from dwarf starburst galaxies. While this mid-IR color selection often fails for the dwarf population, it appears to be quite robust for more luminous galaxies (Stern et al. 2012). From Hainline et al. (2016), it was not clear whether employing the two-color AGN selection of Jarrett et al. (2011) would suffer from contamination as well. They therefore presented a sample of candidate AGNs in dwarf galaxies falling within the color-color AGN selection box of Jarrett et al. (2011) rather than employing a single color cut (Stern et al. 2012). Overall, their results are more in line with findings at optical wavelengths; that is, no enhanced active fraction at low galaxy masses is seen. A subsequent theoretical investigation by Satyapal et al. (2018) also showed that some extreme starbursts with high ionization parameters or gas densities could mimic AGNs in mid-IR color space.

In this paper, we observationally probe the efficacy of the mid-IR *WISE* color-color selection box of Jarrett et al. (2011) in dwarf galaxies using high resolution X-ray and optical/near-IR (NIR) observations with *Chandra* and *HST*. Specifically, we seek to understand whether this AGN selection technique can effectively distinguish between BH activity and star formation when applied to low-mass galaxies.

2. SAMPLE SELECTION

The dwarf galaxies studied here come from the sample of Hainline et al. (2016) that have mid-IR colors suggestive of AGNs. Hainline et al. (2016) start with a sample of $\sim 18,000$ dwarf galaxies ($M_* \lesssim 3 \times 10^9 M_\odot$) in the NASA-Sloan Atlas (v0.1.2)¹ with significant detections in the first three bands of the ALLWISE data release (see Section 2 in Hainline et al. 2016). From this, they identify 41 galaxies with $W1 - W2$ vs. $W2 - W3$ colors that fall within the Jarrett et al. (2011) *WISE* AGN selection box. Eleven of these galaxies have optical emission-line measurements (both redshifts and fluxes) and signal-to-noise ratios > 5 in all four *WISE* bands. We obtained new *Chandra* X-ray Observatory and *Hubble Space Telescope* (*HST*) observations for seven of these dwarf galaxies (Proposal ID: 20700286; PI: Reines) and archival *Chandra* and *HST* observations for three additional galaxies (Proposal ID: 16700103; PI: Reines); the latter are broad-line AGNs/Composites from the Reines et al. (2013) sample and the *Chandra* X-ray + *HST* ultraviolet (UV; $\sim 2700 \text{ \AA}$) observations have previously been presented by Baldassare et al. (2017). The final galaxy had an archival *Chandra* observation, but not *HST* imag-

ing.

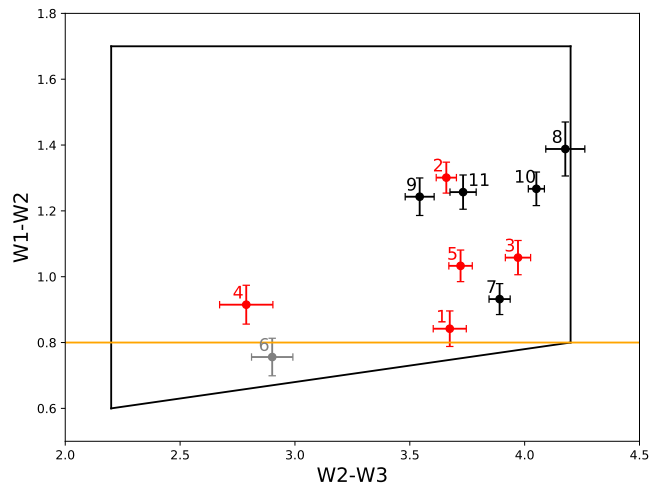


Figure 1. *WISE* color-color diagram for the dwarf galaxies in our sample. The galaxies classified as AGN, composite, and star-forming are in red, grey, and black, respectively, using the $[\text{N II}]/\text{H}\alpha$ BPT diagram (left panel in Figure 2). In black, we plot the AGN selection box from Jarrett et al. (2011), and in orange we show the $W1-W2 > 0.8$ selection criterion from Stern et al. (2012).

Properties of the eleven dwarf galaxies in our sample are summarized in Table 1, and we plot our galaxies on the *WISE* color-color diagram in Figure 1 (see Table 2 for magnitudes). Five of our galaxies are classified as AGNs, one as Composite, and five as star-forming using the $[\text{N II}]/\text{H}\alpha$ BPT diagram (left panel in Figure 2). The line fluxes used for the ratios in Figure 2 are measured from Sloan Digital Sky Survey (SDSS) spectra, as described in Reines et al. (2013). Three-color *HST* images of our galaxies are shown in Figure 3, except in the case of ID 10 for which we use Dark Energy Camera Legacy Survey (DECaLS) imaging.

3. OBSERVATIONS AND DATA REDUCTION

3.1. *Chandra* X-ray Observatory

X-ray observations of our target galaxies were taken with *Chandra* between 2014 Jan 07 and 2020 Jan 03, with exposure times ranging between 8.0 and 24.4 ks. A summary of the *Chandra* observations is given in Table 3. In each observation, the target galaxy was placed at the center of the ACIS S3 chip. We used the CIAO software v4.11 (Fruscione et al. 2006) to reprocess the data and apply calibration files (CALDB 4.8.4.1), creating new level 2 event files.

We next corrected the *Chandra* astrometry by matching to SDSS catalog sources (DR12). We created a list of X-ray point sources by using the CIAO function `wavdetect`, a point source detection algorithm, on the S3 chip of the *Chandra* image filtered from 0.5-7 keV. We excluded any `wavdetect` sources falling within $3r_{50}$ of the galaxy, and used the CIAO function `wcs.match` to match the remaining sources to optical point sources in the SDSS DR12 catalog with i -band magnitudes < 22 . We found between zero and five matching `wavdetect` and SDSS sources on the S3 chip for each observation. We only updated the astrometry if we found at least 1 match, and given the small number of matches, only ap-

¹ <http://nsatlas.org/>

Table 1
Sample of Dwarf Galaxies with Mid-IR Selected Candidate AGNs

ID	BPT Class.	NSAID	RGG ID	SDSS Name	N_{H} (10^{20} cm^{-2})	z	r_{50} (kpc)	M_g (mag)	$g-r$ (mag)	$\log M_{\star}/M_{\odot}$
(1)	(2)	(3)	(4)	(5)	(6)	(7)	(8)	(9)	(10)	(11)
1	AGN	68765	3	J032224.64+401119.8	13.60	0.02679	1.0	-18.7	0.467	9.4
2 ^a	AGN	10779	9	J090613.75+561015.5	2.83	0.04697	1.7	-19.0	0.400	9.4
3 ^a	AGN	125318	11	J095418.15+471725.1	1.03	0.03284	2.0	-18.7	0.438	9.1
4	AGN	113566	18	J114359.58+244251.7	2.09	0.04992	1.3	-18.7	0.647	9.5
5	AGN	104527	24	J133245.62+263449.3	0.99	0.04693	1.2	-19.1	0.272	9.4
6 ^a	Comp.	79874	119	J152637.36+065941.6	3.47	0.03829	0.8	-18.7	0.248	9.3
7	SF	6205	...	J005904.10+010004.2	3.06	0.01743	0.9	-18.3	0.211	8.7
8	SF	98135	...	J154748.99+220303.2	4.64	0.03154	0.7	-18.1	-0.459	8.2
9	SF	57649	...	J160135.95+311353.7	2.72	0.03085	1.3	-18.1	0.109	8.6
10	SF	4610	...	J173501.25+570308.8	3.44	0.04797	0.9	-20.5	-1.050	8.8
11	SF	151888	...	J233244.60-005847.9	4.00	0.02437	1.3	-18.9	0.344	9.3

Note. — Column 1: Identification number used in this paper. Column 2: Classification of the galaxy as AGN, composite (Comp.) or star-forming (SF) from the [N II]/H α BPT diagram (left panel in Figure 2). Column 3: Identification number in the NSA. Column 4: Identification number assigned by Reines et al. (2013). Column 5: SDSS name. Column 6: Galactic neutral hydrogen column density (Dickey & Lockman 1990)^b. Column 7: redshift, specifically the `zdist` parameter from the NSA. Column 8: Petrosian 50% light radius. Column 9: absolute g -band magnitude corrected for foreground Galactic extinction. Column 10: $g-r$ color. Column 11: log galaxy stellar mass. The values given in columns 7-11 are from the NSA and we assume $h = 0.73$.

^aBroad-line AGNs (Baldassare et al. 2017)

^bRetrieved via <https://cxc.harvard.edu/toolkit/colden.jsp>

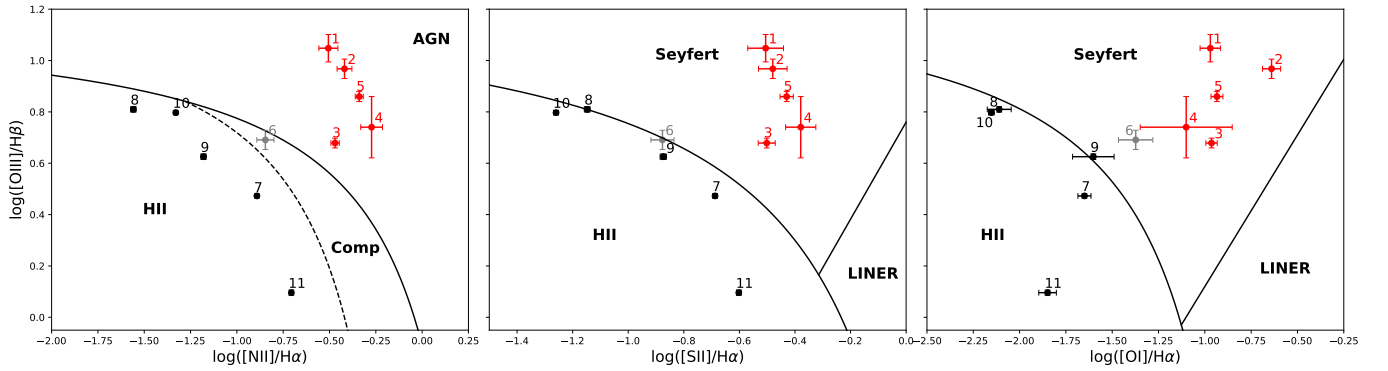


Figure 2. Optical narrow emission line diagnostic diagrams for our galaxies. Regions are separated according to the classification scheme in Kewley et al. (2006). The galaxies falling in the AGN, composite, and star-forming regions in the leftmost diagram are in red, grey, and black, respectively.

Table 2
WISE magnitudes

ID	W1 (mag)	W2 (mag)	W3 (mag)	W1-W2 (mag)	W2-W3 (mag)
(1)	(2)	(3)	(4)	(5)	(6)
1	14.01	13.17	9.50	0.84	3.67
2	13.40	12.10	8.44	1.30	3.66
3	13.86	12.80	8.83	1.06	3.97
4	14.28	13.36	10.57	0.92	2.79
5	13.51	12.48	8.76	1.03	3.72
6	14.12	13.37	10.46	0.76	2.90
7	13.31	12.38	8.49	0.93	3.89
8	15.58	14.20	10.02	1.39	4.18
9	14.53	13.28	9.74	1.24	3.54
10	13.04	11.77	7.72	1.27	4.05
11	13.76	12.50	8.77	1.26	3.73

Table 3
Chandra Observations

ID	Date observed	Obs ID	Exp. time (ks)	$N_{\text{background}}$
1	2019 Mar 26	21446	14.9	0.0070
2	2014 Dec 26	17033	15.8	0.0073
3	2016 Apr 06	17034	8.0	0.0112
4	2019 Mar 10	21447	24.4	0.0057
5	2019 Aug 03	21448	21.8	0.0047
6	2015 Feb 10	17037	10.9	0.0019
7	2019 Sep 20	21449	9.9	0.0085
8	2020 Jan 03	21450	20.8	0.0036
9	2019 Dec 07	21451	19.8	0.0117
10	2014 Jan 07	14908	10.3	0.0015
11	2019 May 08	21452	12.9	0.0144

Note. — $N_{\text{background}}$ is the number of expected 2-10 keV $N(> S)$ background sources within $3r_{50}$, using Moretti et al. (2003).

plied a translation correction. This resulted in updated astrometry for six of the eleven galaxies (IDs 1, 2, 5-6, 8-9), with astrometric shifts ranging between ± 0.02 -1.53 pixels ($0''.01$ - $0''.75$).

3.2. Optical/NIR Images

HST/WFC3 images spanning ultraviolet to NIR wavelengths were taken between 2016 Feb 18 and 2019 Nov 02.

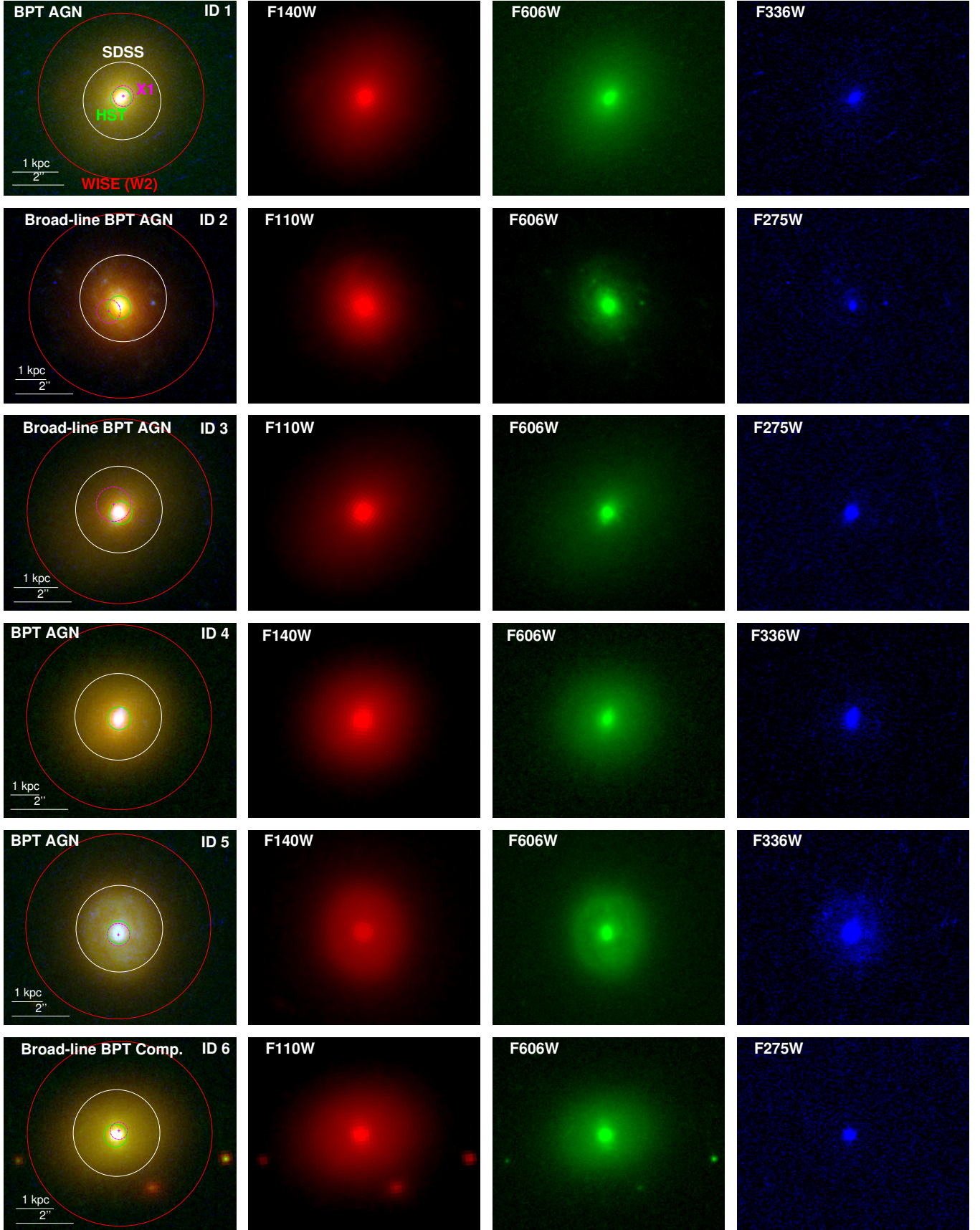


Figure 3. Three-color *HST* images of our galaxies. Red shows the NIR image (F140W for IDs 1,4-5,7-9,11, F110W for IDs 2-3,6), green shows the optical band (F606W), and blue shows the *U*/UV band (F336W for IDs 1,4-5,7-9,11, F275W for IDs 2-3,6). We overlay green circles of radii $0''.4$ at the peak of the NIR emission in the *HST* images, as well as the positions and 95% positional uncertainties of the detected X-ray sources in magenta. The SDSS $3''$ spectroscopic apertures are shown as white circles and the resolution of the *WISE* W2-band ($6.4''$) is in red. The text in the upper left corner denotes the BPT classification of the galaxy. Note that for ID 10, *HST* imaging was unavailable, so DECaLS imaging was used instead, with red, green, and blue as the *z*, *r*, and *g* bands, respectively.

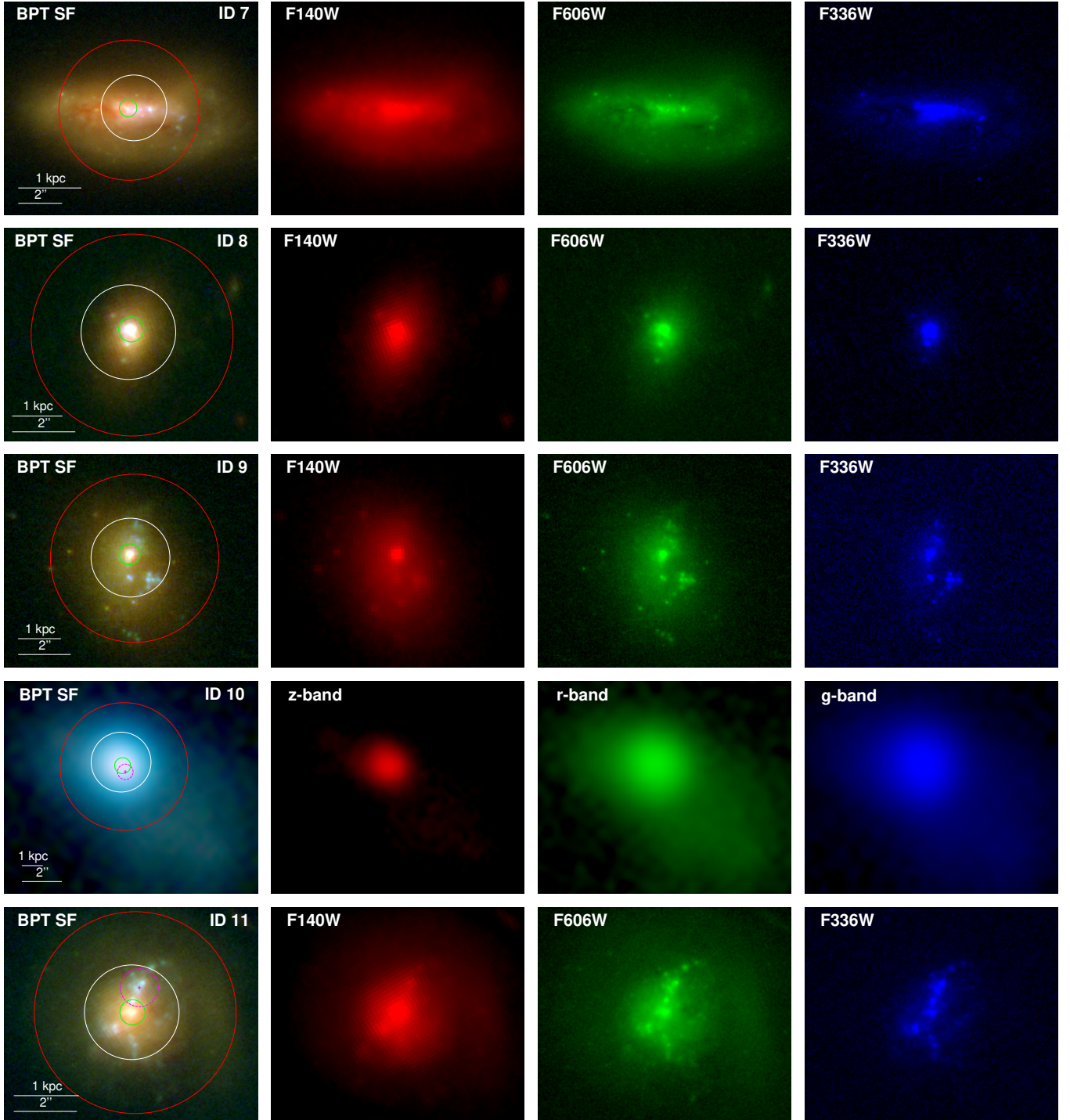


Figure 3. Same as above.

The new data (galaxy IDs 1, 4-5, 7-9, and 11; Proposal 15607, PI: Reines) were taken in the F336W ($\sim U$ -band), F606W (\sim wide V -band), and F140W ($\sim H$ -band) filters. The archival data (galaxy IDs 2-3 and 6; Proposal 13943, PI: Reines) were taken in the F275W (near-UV), F606W, and F110W (\sim wide YJ -band) filters.

Each galaxy was allocated one orbit, with exposure times of ~ 7 -9 minutes in the NIR, ~ 11 -12 minutes in the V -band and ~ 12 -15 minutes in the short wavelength filters. The images were processed using the AstroDrizzle routine in the standard *HST* pipeline. We adjust the astrometry of the *HST* images to match that of the SDSS by comparing common sources between the two, resulting in astrometric shifts up to $0''.52$, with a median shift of $0''.22$. As galaxy ID 10 had no *HST* imaging observations, we retrieved images from DECaLS in the g , r , and z bands for use in Figure 3.

4. ANALYSIS AND RESULTS

4.1. X-ray Sources

Using high-resolution X-ray observations from *Chandra*, we search for X-ray point sources that could indicate the presence of accreting massive BHs in our target dwarf galaxies. We first check our *Chandra* images for background flares, removing time intervals where the background rate was $> 3\sigma$. We then re-run **wavdetect** on images of the S3 chip filtered from 0.5-7 keV. We use wavelet scales of 1.0, 1.4, 2.0, 2.8, and 4.0, with a point spread function map of 39% enclosed energy fraction at 2.3 keV (for hard band; 2-7 keV) and 1.56 keV (for soft band; 0.5-2 keV). We set a significance threshold of 10^{-6} , at which we expect approximately one false source detection over the entire S3 chip. We then restrict further analysis to the **wavdetect** sources that lie within $3r_{50}$ of the galaxy to exclude any X-ray sources not associated with the target.

We find source counts using circular apertures corresponding to the 90% enclosed energy fraction at 4.5 keV ($\sim 2''$ for our sources). We estimate background counts per pixel using circular annuli centered on the source with an inner radius equal to the source aperture radius and an outer radius of $12 \times$ the inner radius. We consider a source to be detected if the source counts are above the background counts in the source aperture to within a 95% confidence level using the Bayesian methods in Kraft et al. (1991) for Poisson-distributed data with low source counts. All detected sources pass this test.

After subtracting off the background counts in the source aperture from the source counts, we apply a 90% aperture correction to arrive at the net counts for each source. We detect a total of seven X-ray point sources across eleven galaxies, and report their properties in Table 4. Note that galaxy IDs 2-3 and 6 were analyzed in Baldassare et al. (2017), and we find the same sources with similar luminosities.

We estimate 95% positional uncertainties using the empirical formula from Hong et al. (2005) involving the **wavdetect** counts and off-axis position of the sources. The error bars on the net counts represent 90% confidence intervals. If the source counts are < 10 , we take the background counts into account and follow the formalism of Kraft et al. (1991). If the source counts are ≥ 10 we use the confidence intervals from Gehrels (1986),

which assume that the background counts are negligible.

We calculate unabsorbed hard (2-10 keV) and soft (0.5-2 keV) X-ray fluxes using the CIAO function **srcflux**. We use a power-law spectral model with photon index $\Gamma = 1.8$, which is typical for low-luminosity AGN (Ho 2008, 2009) and ultraluminous X-ray sources at these energies (Swartz et al. 2008), and Galactic column densities from the Dickey & Lockman (1990) maps. The unabsorbed fluxes and corresponding luminosities are summarized in Table 4. We ignore any potential absorption intrinsic to the sources, so these values should be taken as lower limits.

Finally, we find the expected number of foreground/background hard (soft) X-ray sources to fall within $3r_{50}$ of the galaxy. We use Equation 2 from Moretti et al. (2003) which, given an input flux, returns the expected number of background sources with that flux or higher that we would expect to see (per square degree). As our input fluxes, we use the minimum flux that we would classify as a source; we adopt 2 source counts, corresponding to the dimmest source we detected in each band. The resulting 2-10 keV (0.5-2 keV) minimum fluxes range from $S_{min} \sim 2$ -4.7 (0.7-2) in units of $10^{-15} \text{ erg s}^{-1} \text{ cm}^{-2}$ for our eleven *Chandra* observations. Using these fluxes, we find the expected number of hard band (soft band) background sources within $3r_{50}$ of our galaxies range between ~ 0.001 -0.014 (0.001-0.011).

X-ray sources are detected in seven of our eleven target galaxies (at most one per galaxy) – four BPT AGNs, one composite, and two star-forming galaxies. Six of the seven sources are consistent with being associated with the galaxy nucleus (see Section 4.3 for further discussion). The 2-10 keV X-ray luminosities have a range of $\log(L_{2-10\text{keV}}/\text{erg s}^{-1}) = 39.8$ -41.9 (see Table 4). We use the aforementioned minimum fluxes to provide upper limits on X-ray source luminosities for the remaining four galaxies with non-detections (one BPT AGN and three star-forming galaxies).

As most of our X-ray sources have a low number of counts, we estimate hardness ratios using the Bayesian Estimation of Hardness Ratios code (BEHR; Park et al. 2006), which is useful in the Poisson regime of low counts and works even if only one of the bands has a detection. Hardness ratio here is defined as $(H - S)/(H + S)$, where H and S are the number of detected counts in the hard and soft X-ray bands, respectively. Here, the soft and hard bands correspond to the energy ranges 0.5-2 keV and 2-7 keV, respectively. We have seven galaxies with detections in at least one of the two bands, and the resulting hardness ratios are displayed in Figure 4. We also estimate the hardness ratios using the Portable, Interactive Multi-Mission Simulator (PIMMS)² for absorbed power laws with $\Gamma = 1.8$ and $N_H = 10^{22-24} \text{ cm}^{-2}$ and for unabsorbed power laws with $\Gamma = 1.8, 2.0$, and 2.5 . We plot these in Figure 4 as well.

4.2. Expected Contribution from X-ray Binaries

It can be helpful to establish a rough baseline of how much X-ray luminosity we would expect to see coming from each galaxy in the absence of any AGN – i.e. from

² <https://heasarc.gsfc.nasa.gov/cgi-bin/Tools/w3pimms/w3pimms.pl>

Table 4
X-ray Sources

ID (1)	R.A. (deg) (2)	Decl. (deg) (3)	Net Counts		Flux (10^{-15} erg s $^{-1}$ cm $^{-2}$)		Luminosity (log(erg s $^{-1}$))	
			0.5-2 keV (4)	2-7 keV (5)	0.5-2 keV (6)	2-10 keV (7)	0.5-2 keV (8)	2-10 keV (9)
1	50.602662	40.188872	$6.04^{+5.07}_{-3.46}$	$10.58^{+7.58}_{-4.98}$	4.15	16.21	39.8	40.4
2	136.557572	56.170866	$14.66^{+8.30}_{-5.83}$	$2.02^{+3.62}_{-1.86}$	5.51	2.79	40.4	40.1
3	148.575716	47.290371	$2.07^{+3.66}_{-1.76}$	$2.11^{+3.74}_{-1.83}$	1.69	5.76	39.6	40.1
4 ^a	<0.74	<2.03	<39.6	<40.0
5	203.190100	26.580321	16.82 ± 7.67	$4.09^{+4.48}_{-3.11}$	6.60	4.18	40.5	40.3
6	231.655677	6.994941	484.37 ± 37.9	127.75 ± 20.24	271.89	255.72	41.9	41.9
7 ^a	<1.99	<5.22	<39.1	<39.5
8 ^a	<0.96	<2.42	<39.3	<39.7
9 ^a	<0.94	<2.49	<39.3	<39.7
10	263.755101	57.052294	$13.36^{+7.94}_{-5.50}$	$6.48^{+5.44}_{-3.70}$	6.73	13.58	40.5	40.8
11 ^a	353.187593	-0.979194	...	$3.12^{+4.16}_{-2.48}$	<1.43	5.40	<39.2	39.8

Note. — Column 1: galaxy ID. Column 2: right ascension of X-ray source. Column 3: declination of X-ray source. Columns 4-5: net counts after applying a 90% aperture correction. Error bars represent 90% confidence intervals. Columns 6-7: fluxes corrected for Galactic absorption. Columns 8-9: log luminosities corrected for Galactic absorption; calculated using a photon index of $\Gamma = 1.8$.

^aNo soft and/or hard band X-ray sources were detected in these galaxies. The reported fluxes and luminosities are upper limits (see Section 4.1).

Table 5
Host Galaxy SFRs and Expected Luminosity from XRBs

ID (1)	FUV (mag) (2)	log L(FUV) (erg s $^{-1}$) (3)	W ₂₂ (mag) (4)	log L(22 μ m) (erg s $^{-1}$) (5)	SFR ^{Cor} (M_{\odot} yr $^{-1}$) (6)	SFR ^{Uncor} (M_{\odot} yr $^{-1}$) (7)	12+log O/H (8)
1	21.70	41.3	6.72	42.5	0.60	0.01	8.61
2	20.04	42.5	6.06	43.3	3.46	0.14	8.66
3	19.86	42.2	5.94	43.0	1.90	0.08	8.63
4	23.62	41.1	7.83	42.6	0.74	0.01	8.74
5	20.60	42.3	5.76	43.4	4.46	0.08	8.71
6	20.62	42.1	7.84	42.4	0.48	0.05	8.42
7	18.13	42.4	5.44	42.7	0.92	0.11	8.39
8	18.99	42.6	7.05	42.5	0.76	0.16	8.01
9	20.07	42.1	7.50	42.3	0.44	0.06	8.23
10	16.96	43.7	4.62	43.9	15.5	2.44	8.14
11	17.90	42.8	6.04	42.7	1.17	0.26	8.50

Note. — Column 1: Galaxy identification number used in this paper. Column 2: FUV AB magnitudes from *GALEX* (in the NSA). Column 3: log FUV luminosities. Column 4: *WISE* magnitudes (W4, 22 μ m). Column 5: log 22 μ m luminosities. Column 6: estimated SFRs from *GALEX* and *WISE* data. Column 7: estimated SFRs using only the uncorrected FUV luminosities. Column 8: metallicity estimated using the relation from Pettini & Pagel (2004).

X-ray binaries (XRBs). This expected X-ray luminosity scales with stellar mass for low-mass XRBs (Gilfanov 2004) and with SFR for high-mass XRBs (Grimm et al. 2003). Applying the relation from Gilfanov (2004) between expected X-ray luminosity and stellar mass to our galaxies, we expect a luminosity of at most $\sim 10^{38}$ erg s $^{-1}$ from low-mass XRBs. As this is ~ 1.5 orders of magnitude smaller than the lowest observed X-ray luminosity, we conclude that low-mass XRBs are unlikely to significantly contribute to the luminosity of any of our observed X-ray sources; thus, we focus on high-mass XRBs.

We compare our observed X-ray luminosities to those expected from high-mass XRBs using the model of Lehmer et al. (2021), which relates the expected XRB X-ray luminosity, SFR, and gas-phase metallicity. Figure 5 shows the median values and 16–84% ranges of L_X/SFR as a function of $12 + \log(\text{O}/\text{H})$ from their model (i.e., column 5 of table 3 in Lehmer et al. 2021). Here, L_X refers

to X-ray luminosities in the 0.5–8 keV energy band. To this end, we re-analyze the *Chandra* data for our galaxies in the 0.5–8 keV band, using the same methodology as in Section 4.1. While the 1σ scatter for the Lehmer et al. (2021) relation is metallicity dependent (as evidenced by the changing 16–84% confidence intervals shown in blue in Figure 5), our target galaxies all have $12 + \log(\text{O}/\text{H}) > 8.0$ (see below) and the scatter in this range is less variable with a value of ~ 0.2 dex.

In general, SFRs can be estimated using far-UV (FUV; 1528 Å) and mid-infrared (IR; 25 μ m) luminosities as follows:

$$\begin{aligned} \log \text{SFR}(M_{\odot} \text{ yr}^{-1}) &= \log L(\text{FUV})_{\text{corr}} - 43.35 \\ L(\text{FUV})_{\text{corr}} &= L(\text{FUV})_{\text{obs}} + 3.89 L(25 \mu\text{m}) \end{aligned} \quad (1)$$

(Kennicutt & Evans 2012; Hao et al. 2011). The Hao et al. (2011) sample used to derive $L(\text{FUV})_{\text{corr}}$ in-

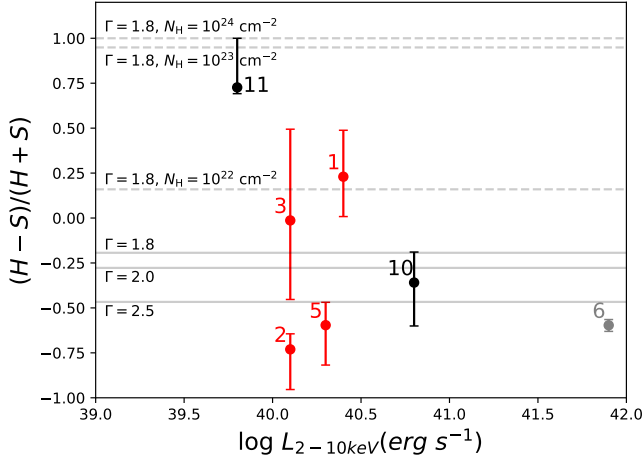


Figure 4. Hardness ratio vs. log 2-10 keV X-ray luminosity for the seven of our galaxies that had a detected X-ray source in at least one of the two bands. The hardness ratio was calculated using BEHR (see Section 4.1). The error bars are the 68% confidence intervals. Galaxies classified as AGN, composite, and star-forming are in red, grey, and black, respectively, based on the $[\text{N II}]/\text{H}\alpha$ BPT diagram. Hardness ratios for unabsorbed power laws with $\Gamma = 1.8$, 2.0, and 2.5 are shown as grey solid lines, while power laws with various absorptions and $\Gamma = 1.8$ are shown as dashed grey lines.

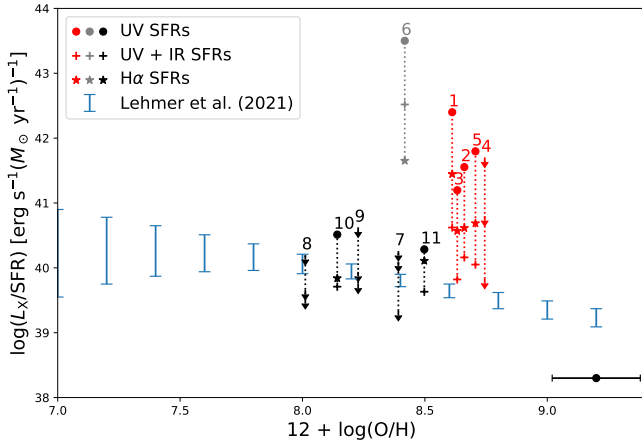


Figure 5. Log ratio of X-ray luminosity over host galaxy SFR vs. metallicity. The crosses represent SFRs calculated with the mid-IR-corrected FUV luminosities, the dots use the uncorrected FUV luminosities (see Equation 1), and the stars use the $\text{H}\alpha$ -derived SFRs - the three are connected by a dotted line for ease of comparison. SFRs based on the mid-IR-corrected FUV luminosities may be severely overestimated if the mid-IR emission is indeed dominated by an AGN as suggested by the *WISE* colors. Similarly, the $\text{H}\alpha$ SFRs are also likely overestimated for the BPT AGNs/Composites since the AGN is contributing to or dominating the line ratios. Arrows indicate upper limits on the X-ray luminosities for galaxies with no significant hard X-ray source detections (calculated from the minimum fluxes). Galaxies classified as AGN, composite, and star-forming are in red, grey, and black, respectively (using the $[\text{N II}]/\text{H}\alpha$ BPT diagram). The values and error bars in blue are the expected X-ray luminosity from XRBs from Lehmer et al. (2021). The ~ 0.18 uncertainty in the metallicities is shown in black in the lower right-hand corner.

cludes normal star-forming galaxies in the local Universe drawn from the *Spitzer* Infrared Nearby Galaxies Survey (SINGS; Kennicutt et al. 2003) and the integrated spectrophotometric survey of Moustakas & Kennicutt (2006). Overall, the FUV and mid-IR luminosities of our target

galaxies fall within the range of these samples (Hao et al. 2011; Kennicutt et al. 2009), albeit at the more sparsely populated low-luminosity end for the FUV. The uncertainty in the resulting SFRs is ~ 0.13 dex.

These equations hold assuming the FUV and mid-IR emission is dominated by star formation. Given that our galaxies have mid-IR colors similar to luminous AGNs, and some show optical evidence for AGNs as well, it is likely that the mid-IR emission is contaminated or even dominated by AGNs in some cases. Therefore we treat SFRs calculated using the relations above as upper limits. We also calculate SFRs using only the FUV data since any potential (mid-IR selected) AGN is less likely to contribute at these short wavelengths. There could still be contamination from AGN emission, which would lead to overestimating the FUV luminosity and thus the SFR. However, this would move galaxies further upwards in Figure 5, resulting in even higher relative observed X-ray luminosities compared to what we would expect from XRBs.

We use FUV magnitudes from the *Galaxy Evolution Explorer* (*GALEX*) and $22\ \mu\text{m}$ magnitudes from *WISE* in place of $25\ \mu\text{m}$ luminosities from the *Infrared Astronomical Satellite* (*IRAS*). The ratio between $22\ \mu\text{m}$ and $25\ \mu\text{m}$ flux densities is expected to be of order one (Jarrett et al. 2013), and while none of our galaxies have *IRAS* detections, all eleven are detected by *WISE*. We summarize the resulting estimates for the SFRs in Table 5. The SFRs estimated from both FUV and mid-IR data (i.e., “corrected SFRs”) span a range of $0.48\text{--}15.50\ M_{\odot}\ \text{yr}^{-1}$, with a median of $0.92\ M_{\odot}\ \text{yr}^{-1}$. The SFRs estimated from the uncorrected FUV luminosities are substantially lower with a range of $0.01\text{--}2.44\ M_{\odot}\ \text{yr}^{-1}$ and a median of $0.08\ M_{\odot}\ \text{yr}^{-1}$.

As an additional check, we also estimate SFRs based on $\text{H}\alpha$ emission in the SDSS spectroscopic fiber using the calibration in Kennicutt & Evans (2012). We use the flux measurements in the NSA and correct for extinction using the Balmer decrement. It is worth noting, however, that the $3''$ fibers do not always cover the full extent of the galaxies, which could result in underestimating the SFRs. On the other hand, AGN emission will artificially boost the $\text{H}\alpha$ luminosities and SFRs for the BPT AGN/Composite galaxies. We find that the $\text{H}\alpha$ -derived SFRs generally fall in between the FUV and FUV+mid-IR SFRs discussed above.

We estimate metallicities via the relation from Pettini & Pagel (2004):

$$12 + \log(\text{O}/\text{H}) = 8.90 + 0.57 \times \log[\text{N II}]/\text{H}\alpha. \quad (2)$$

The 1σ scatter in this relation is 0.18. Using our emission line measurements from SDSS spectroscopy, the metallicities of our targets have a range of $12 + \log(\text{O}/\text{H}) = 8.01\text{--}8.74$, with a median of 8.50 (see Table 5). As this relation is derived from HII regions, it may not provide accurate results when applied to galaxies with AGNs. An AGN would likely increase the $[\text{N II}]/\text{H}\alpha$ flux, thus increasing the derived metallicity. This provides a possible explanation for the separation via metallicity between the BPT AGN and SF galaxies in our sample, as can be seen in Figure 5.

From Figure 5, we can also see that the four BPT AGNs and one composite galaxy with X-ray detections

have X-ray luminosities that are well above the expected contributions from high-mass XRBs when adopting the SFRs derived from FUV data and excluding the mid-IR emission (the latter of which is likely dominated by the AGN). The two BPT star-forming galaxies with X-ray detections have X-ray source luminosities closer to what is expected from XRBs. Specifically, using the FUV SFRs, the BPT AGN/Composite galaxies are $\sim 1.6 - 3.7$ dex higher than expected from the relation of Lehmer et al. (2021), while the BPT star-forming galaxies are $\sim 0.1 - 0.7$ dex higher. In other words, the BPT AGN/Composite galaxies are at least $\sim 8\sigma$ higher than expected, while the BPT SF galaxies are at most $\sim 3.5\sigma$ higher. While these results do not rule out the presence of AGNs in the star-forming galaxies, it certainly does not add confidence to the AGN interpretation for star-forming galaxies with anomalous mid-IR colors. Table 6 summarizes the origin of the X-ray emission in our target galaxies.

The detected X-ray source luminosities are also generally consistent with ultra-luminous X-ray (ULX) sources, which are defined to be off-nuclear X-ray sources with $L_X > 10^{39} \text{ erg s}^{-1}$ (for a recent review of ULXs, see Kaaret et al. 2017). Though ULXs were initially considered strong candidates for typical sub-Eddington accretion onto intermediate-mass BHs (e.g., Sutton et al. 2012), spectroscopic and timing studies now strongly indicate super-Eddington accretion onto stellar mass sources, with several sources clearly identified as neutron stars due to the detection of X-ray pulsations (e.g., Bachetti et al. 2014) or cyclotron absorption features (Brightman et al. 2018). Indeed, based on broadband X-ray spectroscopy, Walton et al. (2018) suggest that the ULX population as a whole might be strongly dominated by neutron star accretors. However, ULXs are rare. ULXs are perhaps viable explanations for the X-ray sources in our BPT star-forming galaxies, though invoking such a scenario is unnecessary since the X-ray luminosities of these galaxies are consistent with the expectations for their X-ray binary population (e.g., Figure 5). We do not consider ULXs likely for the BPT AGN/Composite galaxies since the X-ray sources in these galaxies reside in prominent nuclei with additional multi-wavelength evidence for AGNs.

4.3. Optical/IR Counterparts of the X-ray Sources

Figure 3 shows the *HST* images of our target dwarf galaxies with the X-ray source positions overlaid in magenta (the magenta crosses and circles mark the positions and the 95% positional uncertainties). We also indicate the peak of the NIR emission in the galaxy images using a green circle of radius $0''.4$. The X-ray sources are almost certainly associated with the peak of the NIR emission for the four BPT AGNs (IDs 1-3,5) and one composite galaxy (ID 6) with X-ray detections. In these cases, the positions of the X-ray sources are consistent with prominent nuclei and there are no other obvious alternative optical/NIR counterparts. Of the two star-forming galaxies with detected X-ray sources, IDs 10 and 11, only ID 11 has *HST* imaging allowing us to determine optical counterparts of the X-ray source. In Figure 3 we see that the X-ray source has a larger offset from the peak of the NIR emission, and there are multiple blue (i.e., young) star clusters consistent with the position of the

X-ray source that could host high-mass XRBs. While the X-ray source is consistent with being nuclear for ID 10, we lack *HST* images and are unsure whether or not this galaxy hosts star clusters close to the nucleus.

Given that our targets were selected to have mid-IR *WISE* colors falling in the Jarrett et al. (2011) AGN selected box, we also show the *WISE* W2 angular resolution as a red circle in Figure 3. In all cases, *WISE* is capturing mid-IR emission on galaxy-wide scales and we cannot definitively determine which *HST* sources are physically associated with the mid-IR emission. However, we deem it reasonable to conclude that the mid-IR emission in the BPT AGNs and the composite galaxy is in fact associated with AGNs since these galaxies have low amounts of star formation and compelling evidence for active massive BHs at multiple wavelengths. On the other hand, the mid-IR emission in the BPT star-forming galaxies could certainly be associated with young massive star clusters still partially embedded in their birth cocoons (e.g., Reines et al. 2008). None of the BPT star-forming galaxies have evidence for hosting AGNs other than red mid-IR colors. Moreover, they generally have relatively blue optical colors (Figure 6; also see Hainline et al. 2016) and multiple star clusters visible in the *HST* images, and one (ID 7) has visible extended dust lanes (see Figure 3). Nevertheless, we cannot rule out highly obscured AGNs in these star-forming galaxies, which could also account for the mid-IR colors.

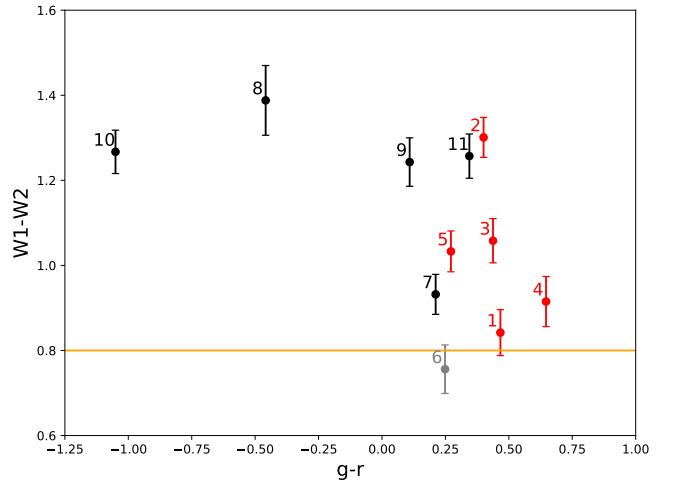


Figure 6. *WISE* W1-W2 color vs. $g-r$ color (from Table 1). The galaxies classified as AGN, composite, and star-forming are in red, grey, and black, respectively, based on the $[\text{N II}]/\text{H}\alpha$ BPT diagram (left panel in Figure 2). In orange we show the $W1-W2 > 0.8$ selection criterion from Stern et al. (2012).

4.4. Multiwavelength AGN Scaling Relations

Here we compare the observed X-ray source luminosities to expectations based on AGN scaling relations for more massive galaxies relating X-ray luminosity to mid-IR luminosity, $\text{H}\alpha$ luminosity and $[\text{O III}]$ luminosity.

4.4.1. L_X vs. L_{IR}

Figure 7 (top panel) shows the relation between $L_{2-10 \text{ keV}}$ and L_{W2} ($4.6 \mu\text{m}$) from Secrest et al. (2015):

Table 6
Multiwavelength Properties of Dwarf Galaxies with Red Mid-IR Colors

ID	BPT Classification	X-ray Source	HST Optical/NIR Counterpart
1	AGN	AGN	prominent nucleus
2	AGN (with broad H α)	AGN	prominent nucleus
3	AGN (with broad H α)	AGN	prominent nucleus
4	AGN	non-detection	...
5	AGN	AGN	prominent nucleus
6	Comp. (with broad H α)	AGN	prominent nucleus
7	SF	non-detection	...
8	SF	non-detection	...
9	SF	non-detection	...
10	SF	XRB/ULX or AGN	unknown (no <i>HST</i>)
11	SF	XRB/ULX or AGN	blue star clusters

Note. — All of our target galaxies were selected to have *WISE* mid-IR colors falling in the Jarrett et al. (2011) AGN selection box. Optical emission lines are measured from SDSS spectroscopy (Reines et al. 2013) and the classification is based on the BPT [O III]/H β vs. [N II]/H α diagnostic diagram. X-ray classifications are based on whether the luminosity exceeds that expected from high-mass XRBs (indicating an AGN) or not (see Section 4.2; the BPT AGN/Composite galaxies are higher than the BPT SF galaxies by at least $\sim 4.5\sigma$). Counterparts of the X-ray sources were determined from the *HST* imaging shown in Figure 3.

$$\log(L_{2-10 \text{ keV}}) = (0.93 \pm 0.03) \cdot \log(L_{W2}) + (3.26 \pm 1.25), \quad (3)$$

where the luminosities are in units of erg s^{-1} and the 1σ scatter is 0.40 dex. This relation was derived from a sample of 184 AGNs detected with *XMM* and *WISE* having both X-ray and mid-IR luminosities $\gtrsim 10^{42} \text{ erg s}^{-1}$. With the exception of ID 6 (a broad-line BPT composite), all of the observed X-ray luminosities and upper limits in our sample are ~ 2 dex lower than the relation between $L_{2-10 \text{ keV}}$ and L_{W2} based on more luminous and massive AGNs. We check this result using the relation from Gandhi et al. (2009), which was derived from a sample of 22 well-resolved AGNs and compares 12 μm luminosity to 2-10 keV X-ray luminosity. For this relation we use W3 fluxes from *WISE* and find similar results; the observed X-ray luminosities are lower than the relation by at least ~ 1.5 dex (except ID 6). We consider three possible explanations for this discrepancy.

First, the mid-IR luminosities could be overestimated (and the sources could be pushed to the right) if there is a significant contribution from star formation. While our *Chandra* X-ray observations have high angular resolution ($\lesssim 1''$), the *WISE* W2 band data has an angular resolution of $6.4''$, which in nearly all cases is roughly on par with the size of the galaxies in our sample. However, we do not expect significant contamination from star formation in the mid-IR for the BPT AGNs (IDs 1-5). In order for these sources to be consistent with the $L_X - L_{\text{IR}}$ relation in Figure 7, we would have to be overestimating the mid-IR AGN luminosities by between 2.0-3.3 dex. This would imply the mid-IR emission is actually dominated by extreme star-formation, which seems highly unlikely given the optical line ratios and X-ray emission are dominated by AGNs. The origin of the mid-IR and X-ray emission in the BPT star-forming galaxies is unclear and may not have anything to do with AGNs.

A second possibility is that the mid-IR emission is dominated by highly obscured AGNs, such that the X-rays are greatly diminished. There are examples of Compton-thick AGNs in low-mass galaxies in the liter-

ature (e.g. Chen et al. 2017; Cann et al. 2020). Under the assumption that an AGN does indeed reside in each of our target galaxies, we can estimate the column density required to suppress the X-ray emission below the $L_X - L_{\text{IR}}$ relation (assuming that intrinsic X-ray luminosity is consistent with said relation). Using PIMMS, we find that the estimated column densities are all (except ID 6) high enough to qualify as Compton-thick with $N_{\text{H}} > 10^{24} \text{ cm}^{-2}$. See Table 7 for specific values and Figure 8 for a visual depiction. However, if Compton-thick AGNs resided in our target galaxies, we would expect to see hints in the X-ray emission. For example, if the AGNs were Compton-thick we would expect more photons at higher energies yielding a positive hardness ratio. Figure 4 demonstrates this is generally not the case. Three of the five BPT AGNs/composites (IDs 2,5,6) fall firmly in the soft range, and two BPT AGNs (IDs 1,3) are ambiguous. While Compton-thick AGNs also typically have strong Fe K α emission, this may not always be the case for heavily obscured and X-ray faint AGNs (see Chen et al. 2017). Nevertheless, using the CIAO function *specextract*, we check both individual and stacked X-ray spectra for the BPT AGN and Composite galaxies with X-ray detections and find no evidence for Fe K α emission. Additionally, broad optical emission lines are generally not observed in obscured AGNs (Hickox & Alexander 2018), and we do see broad H α in three of our X-ray detected AGNs (IDs 2,3,6).

An alternative explanation for the low X-ray luminosities is that the AGNs could be intrinsically X-ray weak (e.g., Dong et al. 2012; Baldassare et al. 2017). It has been proposed that some AGNs in metal-poor host galaxies could simply lack the hard X-ray emission we would expect to see (Simmonds et al. 2016). Similar conclusions have been found regarding AGNs with weak broad lines that are not necessarily obscured (Denney et al. 2014; LaMassa et al. 2015; MacLeod et al. 2016; Hickox & Alexander 2018).

Finally, it is entirely possible that the $L_X - L_{\text{IR}}$ relation simply breaks down at low BH masses or is steeper than has been captured by relations calibrated at higher luminosities. Perhaps these relations cannot be properly

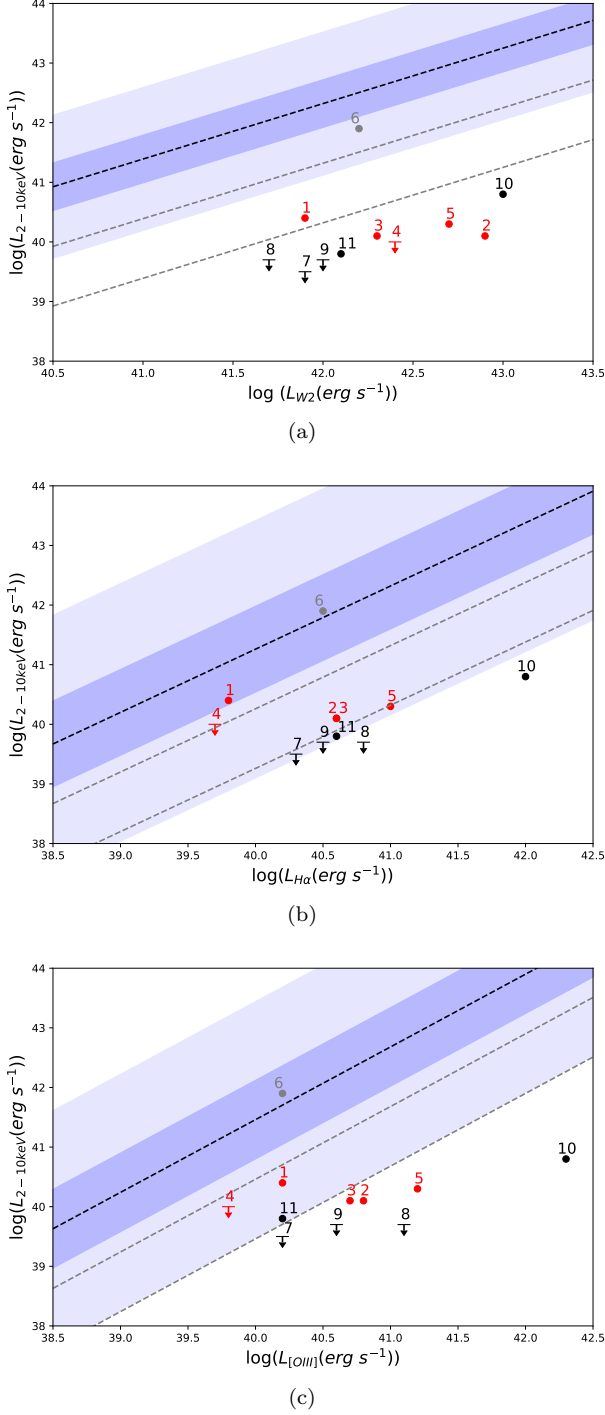


Figure 7. Observed X-ray luminosities vs W2 (top), $H\alpha$ (middle), and [O III] (bottom) luminosities for our galaxies. Galaxies classified as AGN, composite, and star-forming are in red, grey, and black, respectively. The arrows indicate that the X-ray luminosity comes from an upper limit (calculated from minimum fluxes - see Section 4.1). The black dashed lines indicate the expected X-ray luminosity using the Secrest et al. (2015) relation (top, mid-IR; Equation 3) and the relations from Panessa et al. (2006) (middle, $H\alpha$, Equation 4; bottom, [O III], Equation 5). The dark blue shaded areas represent the 1σ scatters and the light blue shaded areas represent the 3σ scatters. The dashed grey lines represent the relations shifted down by 1 and 2 dex, for ease of comparison with the plotted points.

Table 7
Expected L_X from L_{IR}

ID	$W_{4.6}$	$\log W_{4.6}$	$\log L_X^{Obs}$	$\log L_X^{Exp}$	N_H
(1)	(2)	(3)	(4)	(5)	(6)
1	13.17	41.9	40.4	42.3	3.21
2	12.10	42.9	40.1	43.1	6.00
3	12.80	42.3	40.1	42.6	4.60
4	13.36	42.4	<40.0	42.7	>5.14
5	12.48	42.7	40.3	43.0	5.19
6	13.37	42.2	41.9	42.5	0.59
7	12.38	41.9	<39.5	42.2	>5.20
8	14.20	41.7	<39.7	42.0	>4.25
9	13.28	42.0	<39.7	42.3	>5.06
10	11.77	43.0	40.8	43.3	4.56
11	12.50	42.1	39.8	42.4	4.99

Note. — Column 1: Identification number used in this paper. Column 2: *WISE* magnitudes ($W2$, $4.6 \mu m$). Column 3: \log $4.6 \mu m$ ($W2$) luminosities. Column 4: \log observed 2–10 keV X-ray luminosities; galaxy IDs 4, 7–9 had no X-ray detections, so we instead state the calculated minimum detectable luminosities using the minimum observable fluxes (see Section 4.1). Column 5: expected \log 2–10 keV X-ray luminosities, calculated using Equation 3. Column 6: Estimated intrinsic hydrogen column density required to match our observed X-ray luminosities with those predicted by the Secrest et al. (2015) relation (see Equation 3).

extrapolated to dwarf galaxies, where there may be a change in the AGN spectral energy distribution and/or dust properties.

4.4.2. L_X vs. $L_{H\alpha}$ and $L_{[O III]}$

Figure 7 (middle, bottom panels) shows the $L_{2-10 \text{ keV}} - L_{H\alpha}$ and $L_{2-10 \text{ keV}} - L_{[O III]}$ relations from Panessa et al. (2006):

$$\log(L_{2-10 \text{ keV}}) = (1.06 \pm 0.04) \cdot \log(L_{H\alpha}) + (-1.14 \pm 1.78) \quad (4)$$

$$\log(L_{2-10 \text{ keV}}) = (1.22 \pm 0.06) \cdot \log(L_{[O III]}) + (-7.34 \pm 2.53), \quad (5)$$

where the luminosities are in erg s^{-1} . These relations are based on a sample of Seyferts from the Palomar optical spectroscopic survey of nearby galaxies (Ho et al. 1995), and the luminosities ($\log L_X / \text{erg s}^{-1} = 38.2\text{--}43.3$) are measured in the nuclear regions of the galaxies (i.e., not the entire galaxy; Panessa et al. 2006). The $H\alpha$ luminosities used in Panessa et al. (2006) are from the combined narrow and broad (if present) components and are corrected for extinction. We also include both narrow and broad $H\alpha$ components (when detected). While our $H\alpha$ luminosities are not corrected for extinction, this would only increase our luminosities and push them further to the right in Figure 7, thereby increasing the disparity between expected and observed X-ray luminosities.

We estimate the scatter in these relations by taking the standard deviation of the differences between the observed and expected X-ray luminosities of the original sample of Panessa et al. (2006), excluding galaxies that lack detection in one or more of X-ray, $H\alpha$, or [O III] bands (see Table 2 in Panessa et al. 2006). We find a scatter of ~ 0.72 and ~ 0.66 dex for the $H\alpha$ and

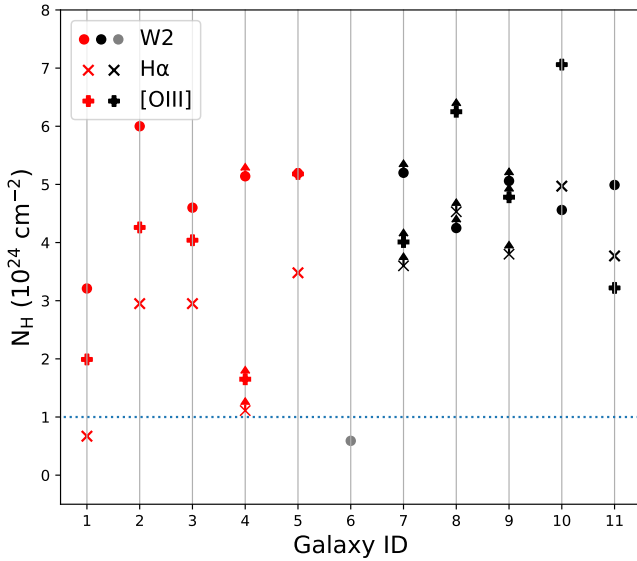


Figure 8. Estimated intrinsic absorption (N_{H}) in each galaxy using the difference between the expected and observed X-ray luminosities. Galaxies classified as AGN, composite, and star-forming are in red, grey, and black, respectively. The dots, x's, and plus signs use the expected X-ray luminosity as calculated from the W2, $\text{H}\alpha$, or $[\text{O III}]$ relations, respectively. The arrows indicate that the observed X-ray luminosity comes from an upper limit calculated from minimum fluxes, which translates into a lower limit for N_{H} . The dotted blue line at $N_{\text{H}} = 10^{24} \text{ cm}^{-2}$ separates out the plot into Compton thick (above the line) and Compton thin (below the line) regions. Note that several estimates of N_{H} are unavailable (e.g. the $\text{H}\alpha$ and $[\text{O III}]$ relations for ID 6) – in these cases, the observed X-ray luminosity was higher than the expected X-ray luminosity, so an estimate was unable to be calculated. Note also that for ID 6, Baldassare et al. (2017) found via spectral fitting that the models did not prefer an N_{H} greater than the Galactic value, suggesting little to no intrinsic absorption.

$[\text{O III}]$ relations, respectively. This does not include uncertainties associated with the fitted parameters in the Panessa et al. (2006) relation.

Our dwarf galaxies are also shown in Figure 7 using our *Chandra* X-ray luminosities and line measurements from SDSS spectroscopy (Reines et al. 2013) – see Tables 8 and 9 for specific values. The points fall systematically below the $L_{\text{X}} - L_{[\text{O III}]}$ and $L_{\text{X}} - L_{\text{H}\alpha}$ relations, but some of the sources are within the 3σ scatter. We note that we do not find any systematic difference between the broad-line and narrow-line AGNs with respect to these relations when considering our sample and the additional broad-line AGNs in dwarf galaxies presented in Baldassare et al. (2017).

Again, we consider various explanations for our targets generally falling below the relations. We do not expect that we are significantly overestimating the line luminosities even though the measurements come from SDSS spectra taken with a $3''$ -aperture (see Figure 3). In order to match the relation, we would have to be overestimating the $\text{H}\alpha$ and $[\text{O III}]$ luminosities of the BPT AGNs by 0.6-1.9 dex and 1.0-2.2 dex, respectively, and therefore star formation would have to dominate the line emission. Given that the line ratios for these galaxies indicate the emission is dominated by AGNs, we rule this scenario out. Similar to the $L_{\text{X}} - L_{\text{IR}}$ relation, we conclude that the $L_{\text{X}} - L_{[\text{O III}]}$ and $L_{\text{X}} - L_{\text{H}\alpha}$ relations are either not applicable to AGNs with low BH masses, which may be

intrinsically X-ray weak, or the relations do not properly extrapolate to dwarf galaxies and may need to be revisited with expanded samples including more such objects.

5. SUMMARY AND CONCLUSIONS

We have presented high-resolution *Chandra* observations of eleven dwarf galaxies having mid-IR selected candidate AGNs culled from the sample of Hainline et al. (2016). Multi-band *HST* observations are also presented for ten of these galaxies. Based on optical SDSS spectroscopy (Reines et al. 2013), five of our target galaxies are classified as BPT AGNs (two of which have broad lines), five as star-forming, and one as Composite (which also has broad lines). Using a suite of multiwavelength diagnostics, we investigate whether mid-IR color-color AGN selection (e.g. Jarrett et al. 2011) is effective when applied to low-mass galaxies. Our primary findings are summarized below (also see Table 6).

1. We detect seven X-ray point sources across our sample of eleven dwarf galaxies, with luminosities in the range $\log(L_{2-10\text{keV}}/\text{erg s}^{-1}) = 39.8\text{--}41.9$. Five of these sources are in BPT AGN or Composite galaxies, and two are in BPT star-forming galaxies.
2. There is strong evidence that the X-ray sources detected in the five optically-selected BPT AGN and Composite galaxies (IDs 1,2,3,5,6) are indeed accreting massive BHs in the nuclei of their host galaxies. The X-ray luminosities are well above the expected contribution from XRBs, and the positions of the X-ray sources are consistent with prominent nuclei, the peak of the NIR emission in the *HST* images, and the centroid of the mid-IR emission from *WISE* (see Figure 3). It is thus reasonable to attribute the detected mid-IR emission from *WISE* to these optically-selected AGNs.
3. The same cannot be said of the BPT star-forming galaxies. Only two of five of these galaxies have X-ray detections (IDs 10,11) and the X-ray luminosities are not so high as to rule out high-mass XRBs. Additionally, *HST* imaging of ID 11 indicates the X-ray source is associated with blue (i.e. young) star clusters that are plausible hosts of an XRB/ULX. The X-ray source in this galaxy is also significantly offset from the peak of the NIR emission and the centroid of the mid-IR emission (see Figure 3), strongly suggesting different origins for the X-ray and mid-IR sources. While the X-ray source in ID 10 is consistent with the nucleus of the galaxy, without *HST* imaging we cannot rule out the possibility of star clusters close to the nucleus, and as such cannot reliably determine the optical counterpart of the X-ray source.
4. We compare the observed X-ray luminosities to those expected from AGN scaling relations using mid-IR, $\text{H}\alpha$, and $[\text{O III}]$ luminosities. In nearly all cases, we find that the observed X-ray emission falls below the relations (see Figure 7), with the largest discrepancies for the $L_{\text{X}} - L_{\text{IR}}$ relation. We consider various explanations and hypothesize that the

Table 8
Expected L_X from $L_{H\alpha}$

ID (1)	$F_{H\alpha}$ (10^{-16} erg s $^{-1}$ cm $^{-2}$) (2)	$\log L_{H\alpha}$ (erg s $^{-1}$) (3)	$\log L_X^{\text{Obs}}$ (erg s $^{-1}$) (4)	$\log L_X^{\text{Exp}}$ (erg s $^{-1}$) (5)	N_H (10^{24} cm $^{-2}$) (6)
1	41.77	39.8	40.4	41.0	0.67
2	53.02	40.6	40.1	41.9	2.95
3	164.28	40.6	40.1	41.9	2.95
4	9.43	39.7	<40.0	40.9	>1.11
5	204.76	41.0	40.3	42.3	3.48
6	49.84	40.5	41.9	41.8	N/A ^a
7	315.78	40.3	<39.5	41.6	>3.60
8	329.23	40.8	<39.7	42.1	>4.53
9	177.75	40.5	<39.7	41.8	>3.80
10	2343.00	42.0	40.8	43.4	4.97
11	368.45	40.6	39.8	41.9	3.77

Note. — Column 1: Identification number used in this paper. Column 2: $H\alpha$ flux. Column 3: $\log H\alpha$ luminosity. This include both narrow and broad (if present) components. Column 4: \log observed 2-10 keV X-ray luminosity. Column 5: expected \log 2-10 keV X-ray luminosity, calculated using Equation 4. Column 6: Estimated intrinsic hydrogen column density required to match our observed X-ray luminosities with those predicted by the Panessa et al. (2006) relation (see Equation 4).

^aEntries of N/A denote a galaxy where the observed X-ray luminosity exceeded the expected X-ray luminosity, so no N_H value could be calculated.

Table 9
Expected L_X from $L_{[\text{O III}]}$

ID (1)	$F_{[\text{O III}]}$ (10^{-16} erg s $^{-1}$ cm $^{-2}$) (2)	$\log L_{[\text{O III}]}$ (erg s $^{-1}$) (3)	$\log L_X^{\text{Obs}}$ (erg s $^{-1}$) (4)	$\log L_X^{\text{Exp}}$ (erg s $^{-1}$) (5)	N_H (10^{24} cm $^{-2}$) (6)
1	111.86	40.2	40.4	41.7	1.99
2	139.83	40.8	40.1	42.4	4.26
3	243.27	40.7	40.1	42.3	4.04
4	11.97	39.8	<40.0	41.2	>1.65
5	390.51	41.2	40.3	43.0	5.18
6	51.16	40.2	41.9	41.7	N/A ^a
7	275.72	40.2	<39.5	41.7	>4.01
8	630.52	41.1	<39.7	42.8	>6.25
9	219.95	40.6	<39.7	42.2	>4.78
10	3969.37	42.3	40.8	44.2	7.06
11	133.58	40.2	39.8	41.7	3.22

Note. — Column 1: Identification number used in this paper. Column 2: $[\text{O III}]$ flux. Column 3: $\log [\text{O III}]$ luminosity. Column 4: \log observed 2-10 keV X-ray luminosity. Column 5: expected \log 2-10 keV X-ray luminosity, calculated using Equation 5. Column 6: Estimated intrinsic hydrogen column density required to match our observed X-ray luminosities with those predicted by the Panessa et al. (2006) relation (see Equation 5).

^aEntries of N/A denote a galaxy where the observed X-ray luminosity exceeded the expected X-ray luminosity, so no N_H value could be calculated.

sources are either intrinsically X-ray weak, or that the scaling relations break down in (or cannot be reliably extrapolated to) the regime of low-mass galaxies/BHs (see Sections 4.4.1 and 4.4.2).

The work of Hainline et al. (2016) demonstrated that using a single *WISE* $W1 - W2$ color cut to select AGN candidates in dwarf galaxies led to severe contamination from young starbursts. Here we show that using a more stringent color-color selection (i.e., Jarrett et al. 2011) still leads to unreliable results for optically-selected star-forming dwarf galaxies. While the WISE color-color selection for our sample of BPT AGN and Composite galaxies seems to be reliable, this mid-IR selection method misses many optically selected AGN and Com-

posite galaxies (see Figure 1 in Hainline et al. 2016). We also demonstrate that $\sim 80 - 90\%$ of the secure mid-IR selected AGNs in our sample (with optical and X-ray evidence for AGNs) have lower than expected X-ray luminosities when compared to multiwavelength scaling relations based on more massive/luminous systems, suggesting these mid-IR selected AGNs are either highly obscured, intrinsically X-ray weak, or that the scaling relations break down when applied to low-mass galaxies such as we have here.

Recently, there have been additional papers analyzing the efficacy of these mid-IR selection techniques. Satyapal et al. (2018) use photoionization and stellar population synthesis models to model AGNs and starbursts,

finding that in some extreme cases these starbursts can have mid-IR colors that would classify them as AGNs using a one-band ($W1 - W2$) color cut (e.g., Stern et al. 2012). They also find that abnormally high ionization parameters or gas densities would be required for a starburst to be classified as an AGN using the two-band color cut of Jarrett et al. (2011), and that these conditions are inconsistent with current observations of star-forming galaxies. Our observational findings presented here suggest such extreme conditions do exist in at least some star-forming dwarf galaxies, or that other physical processes are causing them to fall in the Jarrett et al. (2011) AGN selection box.

Mid-IR AGN selection in dwarfs also has issues due to the relatively poor resolution of *WISE* compared to optical surveys, potentially resulting in contamination due to overlapping sources. Lupi et al. (2020) re-analyzed the sample of Kaviraj et al. (2019), who combined optical and infrared data from the Hyper Suprime-Cam (HSC; Aihara et al. 2017) and *WISE*, respectively, in order to search for AGN in dwarf galaxies. Kaviraj et al. (2019) find an AGN occupation fraction of 10–30% in their sample of ~ 800 galaxies, which is much larger than surveys at other wavelengths. The re-analysis by Lupi et al. (2020) takes into account resolution effects and source overlapping, as HSC has a resolution of $\sim 0''.6$ compared to *WISE* with $\sim 6''$. Lupi et al. (2020) match HSC sources to *WISE* sources (and apply an additional signal-to-noise ratio cut for the $W3$ emission), arriving at a sample of ~ 500 dwarf galaxies. All but 15 of these dwarfs are in groups, with multiple HSC sources associated with one *WISE* source. Assuming the *WISE* source is associated with a dwarf, as opposed to a more luminous galaxy in the group that is also consistent with the *WISE* source, leads to errors in the AGN fraction in dwarf galaxies. Lupi et al. (2020) account for this effect and find an AGN occupation fraction of $\sim 0.4\%$, consistent with other results.

While mid-IR AGN selection in dwarf galaxies at the angular resolution of *WISE* appears to be fraught with problems, mid-IR prospects are likely to improve in the near future. The *James Webb Space Telescope* (*JWST*) will yield significantly higher resolution images in the infrared and facilitate the study of IR coronal emission lines to help identify elusive AGNs (Cann et al. 2018; Satyapal et al. 2020).

We thank the anonymous referee for their helpful comments. Support for this work was provided by NASA through *Chandra* Award Number GO9-20094X issued by the *Chandra X-ray Observatory Center*, which is operated by the Smithsonian Astrophysical Observatory for and on behalf of the NASA under contract NAS8-03060. Based on observations with the NASA/ESA *Hubble Space Telescope* obtained from MAST at the Space Telescope Science Institute, which is operated by the Association of Universities for Research in Astronomy, Incorporated, under NASA contract NAS5-26555. Support for Program number HST-GO-15607.001-A was provided through a grant from the STScI under NASA contract NAS5-26555. AER also acknowledges support for this work provided by NASA through EPSCoR grant number 80NSSC20M0231. The work of DS was carried out at the Jet Propulsion Laboratory, California Institute of

Technology, under a contract with NASA.

The Legacy Surveys consist of three individual and complementary projects: the Dark Energy Camera Legacy Survey (DECaLS; Proposal ID #2014B-0404; PIs: David Schlegel and Arjun Dey), the Beijing-Arizona Sky Survey (BASS; NOAO Prop. ID #2015A-0801; PIs: Zhou Xu and Xiaohui Fan), and the Mayall z-band Legacy Survey (MzLS; Prop. ID #2016A-0453; PI: Arjun Dey). DECaLS, BASS and MzLS together include data obtained, respectively, at the Blanco telescope, Cerro Tololo Inter-American Observatory, NSF’s NOIRLab; the Bok telescope, Steward Observatory, University of Arizona; and the Mayall telescope, Kitt Peak National Observatory, NOIRLab. The Legacy Surveys project is honored to be permitted to conduct astronomical research on Iolkam Du’ag (Kitt Peak), a mountain with particular significance to the Tohono O’odham Nation.

NOIRLab is operated by the Association of Universities for Research in Astronomy (AURA) under a cooperative agreement with the National Science Foundation.

This project used data obtained with the Dark Energy Camera (DECam), which was constructed by the Dark Energy Survey (DES) collaboration. Funding for the DES Projects has been provided by the U.S. Department of Energy, the U.S. National Science Foundation, the Ministry of Science and Education of Spain, the Science and Technology Facilities Council of the United Kingdom, the Higher Education Funding Council for England, the National Center for Supercomputing Applications at the University of Illinois at Urbana-Champaign, the Kavli Institute of Cosmological Physics at the University of Chicago, Center for Cosmology and Astro-Particle Physics at the Ohio State University, the Mitchell Institute for Fundamental Physics and Astronomy at Texas A&M University, Financiadora de Estudos e Projetos, Fundacao Carlos Chagas Filho de Amparo, Financiadora de Estudos e Projetos, Fundacao Carlos Chagas Filho de Amparo a Pesquisa do Estado do Rio de Janeiro, Conselho Nacional de Desenvolvimento Cientifico e Tecnolico and the Ministerio da Ciencia, Tecnologia e Inovacao, the Deutsche Forschungsgemeinschaft and the Collaborating Institutions in the Dark Energy Survey. The Collaborating Institutions are Argonne National Laboratory, the University of California at Santa Cruz, the University of Cambridge, Centro de Investigaciones Energeticas, Medioambientales y Tecnologicas-Madrid, the University of Chicago, University College London, the DES-Brazil Consortium, the University of Edinburgh, the Eidgenossische Technische Hochschule (ETH) Zurich, Fermi National Accelerator Laboratory, the University of Illinois at Urbana-Champaign, the Institut de Ciencies de l’Espai (IEEC/CSIC), the Institut de Fisica d’Altes Energies, Lawrence Berkeley National Laboratory, the Ludwig Maximilians Universitat Munchen and the associated Excellence Cluster Universe, the University of Michigan, NSF’s NOIRLab, the University of Nottingham, the Ohio State University, the University of Pennsylvania, the University of Portsmouth, SLAC National Accelerator Laboratory, Stanford University, the University of Sussex, and Texas A&M University.

BASS is a key project of the Telescope Access Program (TAP), which has been funded by the National Astronomical Observatories of China, the Chi-

nese Academy of Sciences (the Strategic Priority Research Program “The Emergence of Cosmological Structures” Grant # XDB09000000), and the Special Fund for Astronomy from the Ministry of Finance. The BASS is also supported by the External Cooperation Program of Chinese Academy of Sciences (Grant # 114A11KYSB20160057), and Chinese National Natural Science Foundation (Grant # 11433005).

The Legacy Survey team makes use of data products from the Near-Earth Object Wide-field Infrared Survey Explorer (NEOWISE), which is a project of the Jet Propulsion Laboratory/California Institute of Technology. NEOWISE is funded by the National Aeronautics and Space Administration.

The Legacy Surveys imaging of the DESI footprint is supported by the Director, Office of Science, Office of High Energy Physics of the U.S. Department of Energy under Contract No. DE-AC02-05CH1123, by the National Energy Research Scientific Computing Center, a DOE Office of Science User Facility under the same contract; and by the U.S. National Science Foundation, Division of Astronomical Sciences under Contract No. AST-0950945 to NOAO.

REFERENCES

- Aihara, H., Armstrong, R., Bickerton, S., et al. 2017, *Publications of the Astronomical Society of Japan*, 70, doi: 10.1093/pasj/psx081
- Bachetti, M., Harrison, F. A., Walton, D. J., et al. 2014, *Nature*, 514, 202, doi: 10.1038/nature13791
- Baldassare, V. F., Geha, M., & Greene, J. 2018, *ApJ*, 868, 152, doi: 10.3847/1538-4357/aac6cf
- Baldassare, V. F., Geha, M., & Greene, J. 2020, *The Astrophysical Journal*, 896, 10, doi: 10.3847/1538-4357/ab8936
- Baldassare, V. F., Reines, A. E., Gallo, E., & Greene, J. E. 2015, *The Astrophysical Journal Letters*, 809, L14, doi: 10.3847/2041-8205/809/i=1/a=L14
- . 2017, *The Astrophysical Journal*, 836, 20, doi: 10.3847/1538-4357/836/1/20
- Baldassare, V. F., Reines, A. E., Gallo, E., et al. 2016, *The Astrophysical Journal*, 829, 57, doi: 10.3847/1538-4357/829/i=1/a=57
- Birchall, K. L., Watson, M. G., & Aird, J. 2020, *Monthly Notices of the Royal Astronomical Society*, 492, 2268, doi: 10.1093/mnras/staa040
- Brightman, M., Harrison, F. A., Fürst, F., et al. 2018, *Nature Astronomy*, 2, 312, doi: 10.1038/s41550-018-0391-6
- Cann, J. M., Satyapal, S., Abel, N. P., et al. 2018, *ApJ*, 861, 142, doi: 10.3847/1538-4357/aac64a
- Cann, J. M., Satyapal, S., Bohn, T., et al. 2020, *The Astrophysical Journal*, 895, 147, doi: 10.3847/1538-4357/ab8b64
- Chen, C.-T. J., Brandt, W. N., Reines, A. E., et al. 2017, *The Astrophysical Journal*, 837, 48, doi: 10.3847/1538-4357/aa5d5b
- Denney, K. D., Rosa, G. D., Croxall, K., et al. 2014, *The Astrophysical Journal*, 796, 134, doi: 10.1088/0004-637x/796/2/134
- Dickey, C., Geha, M., Wetzel, A., & El-Badry, K. 2019, *arXiv e-prints*. <https://arxiv.org/abs/1902.01401>
- Dickey, J. M., & Lockman, F. J. 1990, *ARA&A*, 28, 215, doi: 10.1146/annurev.aa.28.090190.001243
- Dong, R., Greene, J. E., & Ho, L. C. 2012, *The Astrophysical Journal*, 761, 73, doi: 10.1088/0004-637x/761/1/73
- Fruscione, A., McDowell, J. C., Allen, G. E., et al. 2006, in *Society of Photo-Optical Instrumentation Engineers (SPIE) Conference Series*, Vol. 6270, Society of Photo-Optical Instrumentation Engineers (SPIE) Conference Series, 1, doi: 10.1117/12.671760
- Gandhi, P., Horst, H., Smette, A., et al. 2009, *A&A*, 502, 457, doi: 10.1051/0004-6361/200811368
- Gehrels, N. 1986, *ApJ*, 303, 336, doi: 10.1086/164079
- Gilfanov, M. 2004, *Monthly Notices of the Royal Astronomical Society*, 349, 146, doi: 10.1111/j.1365-2966.2004.07473.x
- Greene, J. E. 2012, *Nature Communications*, 3, 1304 EP, doi: 10.1038/ncomms2314
- Greene, J. E., Strader, J., & Ho, L. C. 2020, *Annual Review of Astronomy and Astrophysics*, 58, 257, doi: 10.1146/annurev-astro-032620-021835
- Griffith, R. L., Tsai, C.-W., Stern, D., et al. 2011, *The Astrophysical Journal*, 736, L22, doi: 10.1088/2041-8205/736/L1/22
- Grimm, H.-J., Gilfanov, M., & Sunyaev, R. 2003, *Monthly Notices of the Royal Astronomical Society*, 339, 793, doi: 10.1046/j.1365-8711.2003.06224.x
- Hainline, K. N., Reines, A. E., Greene, J. E., & Stern, D. 2016, *The Astrophysical Journal*, 832, 119, doi: 10.3847/1538-4357/832/i=2/a=119
- Hao, C.-N., Kennicutt, R. C., Johnson, B. D., et al. 2011, *The Astrophysical Journal*, 741, 124, doi: 10.3847/1538-4357/741/i=2/a=124
- Hickox, R. C., & Alexander, D. M. 2018, *Annual Review of Astronomy and Astrophysics*, 56, 625, doi: 10.1146/annurev-astro-081817-051803
- Hirashita, H., & Hunt, L. K. 2004, *A&A*, 421, 555, doi: 10.1051/0004-6361:20035835
- Ho, L. C. 2008, *ARA&A*, 46, 475, doi: 10.1146/annurev.astro.46.051806.110546
- . 2009, *ApJ*, 699, 626, doi: 10.1088/0004-637x/699/1/626
- Ho, L. C., Filippenko, A. V., & Sargent, W. L. 1995, *ApJS*, 98, 477, doi: 10.1086/192170
- Hong, J., van den Berg, M., Schlegel, E. M., et al. 2005, *ApJ*, 635, 907, doi: 10.1086/496966
- Izotov, Y. I., Guseva, N. G., Fricke, K. J., & Henkel, C. 2011, *A&A*, 536, L7, doi: 10.1051/0004-6361/201118402
- Izotov, Y. I., Guseva, N. G., Fricke, K. J., Krügel, E., & Henkel, C. 2014, *A&A*, 570, A97, doi: 10.1051/0004-6361/201423539
- Jarrett, T. H., Cohen, M., Masci, F., et al. 2011, *The Astrophysical Journal*, 735, 112, doi: 10.1088/0004-637x/735/2/112
- Jarrett, T. H., Masci, F., Tsai, C. W., et al. 2013, *The Astronomical Journal*, 145, 6, doi: 10.1088/1538-3881/145/i=1/a=6
- Kaaret, P., Feng, H., & Roberts, T. P. 2017, *ARA&A*, 55, 303, doi: 10.1146/annurev-astro-091916-055259
- Kaviraj, S., Martin, G., & Silk, J. 2019, *Monthly Notices of the Royal Astronomical Society: Letters*, 489, L12, doi: 10.1093/mnrasl/slz102
- Kennicutt, Robert C., J., Armus, L., Bendo, G., et al. 2003, *PASP*, 115, 928, doi: 10.1086/376941
- Kennicutt, Robert C., J., Hao, C.-N., Calzetti, D., et al. 2009, *ApJ*, 703, 1672, doi: 10.1088/0004-637x/703/2/1672
- Kennicutt, R. C., & Evans, N. J. 2012, *Annual Review of Astronomy and Astrophysics*, 50, 531, doi: 10.1146/annurev-astro-081811-125610
- Kewley, L. J., Groves, B., Kauffmann, G., & Heckman, T. 2006, *Monthly Notices of the Royal Astronomical Society*, 372, 961, doi: 10.1111/j.1365-2966.2006.10859.x
- Kraft, R. P., Burrows, D. N., & Nousek, J. A. 1991, *ApJ*, 374, 344, doi: 10.1086/170124
- LaMassa, S. M., Cales, S., Moran, E. C., et al. 2015, *The Astrophysical Journal*, 800, 144, doi: 10.1088/0004-637x/800/2/144
- Latimer, L. J., Reines, A. E., Plotkin, R. M., Russell, T. D., & Condon, J. J. 2019, *The Astrophysical Journal*, 884, 78, doi: 10.3847/1538-4357/ab3289
- Lehmer, B. D., Eufrazio, R. T., Basu-Zych, A., et al. 2021, *ApJ*, 907, 17, doi: 10.3847/1538-4357/abce1
- Lemons, S. M., Reines, A. E., Plotkin, R. M., Gallo, E., & Greene, J. E. 2015, *The Astrophysical Journal*, 805, 12, doi: 10.3847/1538-4357/805/i=1/a=12
- Lupi, A., Sbarrato, T., & Carniani, S. 2020, *Monthly Notices of the Royal Astronomical Society*, 492, 2528, doi: 10.1093/mnras/stz3636
- MacLeod, C. L., Ross, N. P., Lawrence, A., et al. 2016, *Monthly Notices of the Royal Astronomical Society*, 457, 389, doi: 10.1093/mnras/stv2997
- Marleau, F. R., Clancy, D., Habas, R., & Bianconi, M. 2017, *A&A*, 602, A28, doi: 10.1051/0004-6361/201629832
- Mezcua, M. 2017, *International Journal of Modern Physics D*, 26, 1730021, doi: 10.1142/S021827181730021X
- Mezcua, M., Civano, F., Marchesi, S., et al. 2018, *Monthly Notices of the Royal Astronomical Society*, 478, 2576, doi: 10.1093/mnras/sty1163
- Mezcua, M., & Sánchez, H. D. 2020, *The Astrophysical Journal*, 898, L30, doi: 10.3847/2041-8213/aba199
- Mezcua, M., Suh, H., & Civano, F. 2019, *Monthly Notices of the Royal Astronomical Society*, 488, 685, doi: 10.1093/mnras/stz1760
- Moran, E. C., Shahinyan, K., Sugarman, H. R., Vélez, D. O., & Eracleous, M. 2014, *The Astronomical Journal*, 148, 136, doi: 10.1088/1538-3881/148/i=6/a=136
- Moretti, A., Campana, S., Lazzati, D., & Tagliaferri, G. 2003, *ApJ*, 588, 696, doi: 10.1086/374335
- Moustakas, J., & Kennicutt, Robert C., J. 2006, *ApJS*, 164, 81, doi: 10.1086/500971

- Nguyen, D. D., Seth, A. C., Neumayer, N., et al. 2019, *ApJ*, 872, 104, doi: 10.3847/1538-4357/aafe7a
- O'Connor, J. A., Rosenberg, J. L., Satyapal, S., & Secrest, N. J. 2016, *Monthly Notices of the Royal Astronomical Society*, 463, 811, doi: 10.1093/mnras/stw1976
- Panessa, F., Bassani, L., Cappi, M., et al. 2006, *A&A*, 455, 173, doi: 10.1051/0004-6361:20064894
- Pardo, K., Goulding, A. D., Greene, J. E., et al. 2016, *The Astrophysical Journal*, 831, 203, <http://stacks.iop.org/0004-637X/831/i=2/a=203>
- Park, T., Kashyap, V. L., Siemiginowska, A., et al. 2006, *ApJ*, 652, 610, doi: 10.1086/507406
- Pettini, M., & Pagel, B. E. J. 2004, *MNRAS*, 348, L59, doi: 10.1111/j.1365-2966.2004.07591.x
- Reines, A. E., & Comastri, A. 2016, *Publications of the Astronomical Society of Australia*, 33, e054, doi: 10.1017/pasa.2016.46
- Reines, A. E., Condon, J. J., Darling, J., & Greene, J. E. 2020, *The Astrophysical Journal*, 888, 36, doi: 10.3847/1538-4357/ab4999
- Reines, A. E., Greene, J. E., & Geha, M. 2013, *The Astrophysical Journal*, 775, 116, <http://stacks.iop.org/0004-637X/775/i=2/a=116>
- Reines, A. E., Johnson, K. E., & Goss, W. M. 2008, *The Astronomical Journal*, 135, 2222, <http://stacks.iop.org/1538-3881/135/i=6/a=2222>
- Reines, A. E., Plotkin, R. M., Russell, T. D., et al. 2014, *The Astrophysical Journal Letters*, 787, L30, <http://stacks.iop.org/2041-8205/787/i=2/a=L30>
- Reines, A. E., Sivakoff, G. R., Johnson, K. E., & Brogan, C. L. 2011, *Nature*, 470, 66 EP, <http://dx.doi.org/10.1038/nature09724>
- R  my-Ruyer, A., Madden, S. C., Galliano, F., et al. 2015, *A&A*, 582, A121, doi: 10.1051/0004-6361/201526067
- Ricarte, A., & Natarajan, P. 2018, *MNRAS*, 481, 3278, doi: 10.1093/mnras/sty2448
- Sartori, L. F., Schawinski, K., Treister, E., et al. 2015, *Monthly Notices of the Royal Astronomical Society*, 454, 3722, doi: 10.1093/mnras/stv2238
- Satyapal, S., Abel, N. P., & Secrest, N. J. 2018, *The Astrophysical Journal*, 858, 38, doi: 10.3847/1538-4357/aab7f8
- Satyapal, S., Kamal, L., Cann, J. M., Secrest, N. J., & Abel, N. P. 2020, *arXiv e-prints*, arXiv:2009.05362, <https://arxiv.org/abs/2009.05362>
- Satyapal, S., Secrest, N. J., McAlpine, W., et al. 2014, *The Astrophysical Journal*, 784, 113, doi: 10.1088/0004-637x/784/2/113
- Schramm, M., Silverman, J. D., Greene, J. E., et al. 2013, *The Astrophysical Journal*, 773, 150, <http://stacks.iop.org/0004-637X/773/i=2/a=150>
- Schutte, Z., Reines, A. E., & Greene, J. E. 2019, *The Astrophysical Journal*, 887, 245, doi: 10.3847/1538-4357/ab35dd
- Secrest, N. J., Satyapal, S., Gliozzi, M., et al. 2015, *ApJ*, 798, 38, doi: 10.1088/0004-637X/798/1/38
- Simmonds, C., Bauer, F. E., Thuan, T. X., et al. 2016, *A&A*, 596, A64, doi: 10.1051/0004-6361/201629310
- Stern, D., Assef, R. J., Benford, D. J., et al. 2012, *The Astrophysical Journal*, 753, 30, doi: 10.1088/0004-637x/753/1/30
- Sutton, A. D., Roberts, T. P., Walton, D. J., Gladstone, J. C., & Scott, A. E. 2012, *MNRAS*, 423, 1154, doi: 10.1111/j.1365-2966.2012.20944.x
- Swartz, D. A., Soria, R., & Tennant, A. F. 2008, *The Astrophysical Journal*, 684, 282, doi: 10.1086/587776
- van Wassenhove, S., Volonteri, M., Walker, M. G., & Gair, J. R. 2010, *MNRAS*, 408, 1139, doi: 10.1111/j.1365-2966.2010.17189.x
- Vito, F., Brandt, W. N., Yang, G., et al. 2018, *MNRAS*, 473, 2378, doi: 10.1093/mnras/stx2486
- Volonteri, M. 2010, *The Astronomy and Astrophysics Review*, 18, 279, doi: 10.1007/s00159-010-0029-x
- Volonteri, M., & Reines, A. E. 2016, *ApJ*, 820, L6, doi: 10.3847/2041-8205/820/1/L6
- Walton, D. J., F  rst, F., Heida, M., et al. 2018, *ApJ*, 856, 128, doi: 10.3847/1538-4357/aab610
- Wright, E. L., Eisenhardt, P. R. M., Mainzer, A. K., et al. 2010, *AJ*, 140, 1868, doi: 10.1088/0004-6256/140/6/1868